Hindawi
International Journal of Energy Research
Volume 2023, Article ID 6327620, 14 pages
https://doi.org/10.1155/2023/6327620

Research Article

Cr-Doped NiCo-Layered Double Hydroxide/N-Doped Graphene for a Bifunctional Electrocatalyst for Rechargeable Zinc Air Batteries

Dong Wook Kim,[1,2] **Beum Jin Park**,[1] **Youngkwon Kim**,[1] **and Ho Seok Park**[2]

[1]*Advanced Batteries Research Center, Korea Electronics Technology Institute, 25, Saenari-ro, Seongnam 13509, Republic of Korea*
[2]*School of Chemical Engineering, Sungkyunkwan University, 2066, Seobu-ro, Jangan-gu, Suwon 16419, Republic of Korea*

Correspondence should be addressed to Youngkwon Kim; ykkim96@keti.re.kr and Ho Seok Park; phs0727@skku.edu

Received 17 October 2022; Revised 3 December 2022; Accepted 5 December 2022; Published 3 February 2023

Academic Editor: Kisan Chhetri

Rechargeable zinc air batteries (RZABs), which repeatedly store and release charges through the oxygen evolution reaction (OER) and oxygen reduction reaction (ORR) using oxygen electrocatalysts, are considered a promising energy storage system owing to their low cost and safety. Controlling the chemical structure and morphology of multifunctional electrocatalysts is crucial for improving their electrocatalytic activities and stabilities for high performance RZABs. Herein, we report hierarchically structured Cr-doped NiCo-layered double hydroxides (LDHs) nanoplates chemically grown on the surface of nitrogen-doped reduced graphene oxide nanosheets (NiCoCr LDH/N-rGO) for an application into bifunctional electrocatalysts of RZABs. As verified by the spectroscopic and electrochemical characterizations, Cr doping modulates the electronic configuration and surface structure of both LDHs and N-rGO nanosheets, thereby improving bifunctional catalytic activity and reaction kinetics. In particular, the electrocatalytic activity and kinetics of NiCoCr LDH/N-rGO for both ORR and OER are greatly improved owing to the increased active sites by Cr doping and hierarchical porous structure as demonstrated by low overpotential and Tafel's slope. Thus, the electrochemical performance of RZAB with NiCoCr LDH/N-rGO catalyst is superior to that with Pt/C $+RuO_2$, as confirmed by higher power density of 97 mW cm^{-2} and better cycling stability of 18 h for the former than 59 mW cm^{-2} and 6 h for the latter.

1. Introduction

Among the various energy conversion and storage systems, the rechargeable zinc air batteries (RZABs) are promising energy storage systems, owing to their reliable safety, cost effectiveness, high specific energy density, and easy manufacture [1]. RZABs can charge through the oxygen evolution reaction (OER) and discharge via the oxygen reduction reaction (ORR) in a repeated manner, delivering a high gravimetric energy density of 1,350 Wh kg^{-1}, which is four times higher than that of commercial LIB. Considering that RZABs are featured with an aqueous rechargeable battery that use an inflammable, inexpensive, and nontoxic aqueous electrolyte, they are conducive to the manufacturing process as it can be assembled under atmospheric environment [2].

However, there is an inherent disadvantage in the commercialization of RZABs owing to their energy storage mechanism. RZABs are based on oxygen evolution and reduction reactions during battery charging and discharging, respectively; therefore, the high energy barrier should be overcome through the introduction of electrocatalysts for the OER and ORR [3]. To minimize the overpotential of OER and ORR, noble metal-based electrocatalysts, such as Pt, Ir, and Ru, have been used as OER and ORR catalysts because of their high activity. Unfortunately, commercial noble metal-based electrocatalysts suffer from inferior stability when used in alkaline electrolytes of RZAB, which is attributed to nanoparticle agglomeration and carbon corrosion [4]. Therefore, developing alternatives to noble metal-based materials is crucial for the commercialization of RZABs. In particular, bifunctional

electrocatalysts could be an effective way to commercialize RZABs because of the advantages of reduced manufacturing cost and decreased volume and weight of the device to achieve high energy density [5].

Among the various nonnoble metal electrocatalysts, layered double hydroxides (LDH) are promising for the electrocatalysis of OER [6]. LDH is a two-dimensional (2D) layered structure material, which consists of a metal hydroxide layer with a positive charge originating from the charge difference between bivalent and trivalent metal ions and guest anions for charge balancing and water molecules in the interlayer space. The tunable chemical compositions and structures of the metal hydroxide layer and exchangeable guest anions make LDH suitable electrocatalysts for the OER [7, 8]. However, there are critical drawbacks in LDH that can be directly applied to RZABs; these include particle aggregation and low electrical conductivity. In addition, LDH is known as a material with poor ORR activity, which can be a critical problem for application to RZABs, which utilize the ORR reaction during the discharging process. Therefore, chemical modifications, such as introducing dopants into the metal hydroxide layer for the enhanced catalytic activity or compositing with conductive carbon nanomaterials for the improved electrical conductivity, are required to overcome the aforementioned problems [9].

Nitrogen-doped graphene oxide acts as an ORR electrocatalyst with high electrocatalytic activity as well as a conducting substrate to modify LDHs. Various nitrogen species in nitrogen-doped carbon materials, such as pyridinic and pyrrolic N, can effectively enhance the ORR catalytic activity. Pyridinic N has a pair of electrons and electrons donated to the conjugated π bond in carbon, which facilitates the adsorption of O_2. In addition, the nitrogen dopant element in carbon could enhance the ORR activity, owing to the increased electron density of states in the vicinity of the Fermi level of nitrogen-doped carbon materials [10].

In this study, NiCoCr LDH/N-rGO was synthesized as a bifunctional electrocatalyst for the air cathode of RZABs. Herein, nitrogen-doped graphene oxide (N-rGO) was regarded as both support materials for LDH and electrocatalyst for the ORR [11]. Dopant element Cr was introduced to the LDH hydroxide layer to further enhance the electrocatalytic activity for both OER and ORR. Benefiting from the doping of Cr into LDH, Cr could induce additional active sites for OER and ORR by increasing the surface disorder and oxygen vacancies in LDH/N-rGO composite materials and regulating the electronic configuration of transition metal cations, thus leading to enhanced catalytic performance. The as-prepared NiCoCr LDH/N-rGO could be a possible bifunctional electrocatalyst for RZABs, owing to its appropriate electrocatalytic performance for the OER, ORR, and battery performance. The RZAB using NiCoCr LDH/N-rGO as a bifunctional electrocatalyst exhibited superior rate capability and cycle stability compared to Pt/C+RuO_2 and NiCo LDH/N-rGO, which is consistent with the results of the RDE electrochemical test. Consequently, the doping of Cr into LDH and chemical composites with N-rGO could be an effective method to enhance the OER and ORR electrocatalytic performance of RZAB.

2. Experimental Methods

2.1. Synthesis of NiCoCr LDH/N-rGO. In this work, 98.0% $Ni(NO_3)_2 \cdot 6H_2O$ (Sigma Aldrich, USA), 98.0% $Co(NO_3)_2 \cdot 6H_2O$ (Sigma Aldrich, USA), 98.0% $CrCl_3 \cdot 6H_2O$ (Sigma Aldrich, USA), methyl alcohol (Daejung, South Korea), 0.5 wt% graphene oxide (GO) aqueous dispersion (Daejung, South Korea), and 28.0~30.0% ammonia solution (Junsei Chemical, Japan) were used without further purification. First, GO solution (40 ml) and ammonia solution (8 ml) were dispersed in 40 ml of distilled water (DIW) using ultrasonication for 1 h. Subsequently, the above solution was transferred to a 100 ml Teflon coated autoclave and treated at 120°C for 8 h through a hydrothermal reaction. Following the hydrothermal treatment, the obtained solution was centrifuged and washed with DIW and ethanol until neutral pH was reached. The washed N-rGO suspension was redispersed in methanol and DIW solution (solution A). Thereafter, 0.5 g of 98.0% $Ni(NO_3)_2 \cdot 6H_2O$ (Sigma Aldrich, USA), 1.86 g of 98.0% $Co(NO_3)_2 \cdot 6H_2O$ (Sigma Aldrich, USA), and 0.14 g of 98.0% $CrCl_3 \cdot 6H_2O$ (Sigma Aldrich, USA) were dissolved in 250 ml of methanol and DIW solution (solution B). Subsequently, 70 ml of solution B was added dropwise to solution A under vigorous stirring. After stirring for 30 min, the mixed solution was transferred to a 200 ml Teflon coated autoclave and treated at 180°C for 18 h through a hydrothermal reaction. The as-obtained suspension was centrifuged and washed with DIW and ethanol. Finally, the precipitates were dipped into liquid nitrogen and freeze dried for 3 days to obtain the NiCoCr LDH/N-rGO composite powders.

2.2. Materials Characterization. The size, thickness, and morphology of the samples were examined by using field emission scanning electron microscopy (FE-SEM, JEOL JMS-7000F). The morphology and crystallographic structural information of materials were obtained from high-resolution transmission electron microscopy (HR-TEM, JEOL, ARM-200F), using Lacey carbon type A 300 mesh copper grid. Crystal structural properties of the composite materials were analyzed by X-ray diffraction (XRD, PANalytical, Emprean) using an X-ray source of Cu K_α with a wavelength of 1.5406 Å. The micro-Raman spectrometer (Bruker, SENTERRA) with a laser beam wavelength of 532 nm was used to measure spectroscopic information of materials. The Brunauer-Emmett-Teller (BET) specific surface area and N_2 adsorption-desorption isotherms of the materials were measured by a gas analyzer (Micrometics, TriStar II 3020) at 78 K. The Barrett-Joyner-Halenda (BJH) analysis was used to evaluate the distribution of pore sizes of materials. The information of chemical structure and environment of the surface of materials was obtained by using X-ray photoelectron spectroscopy (XPS, Thermo-Scientific, K_α) analysis with referencing the C 1 s peak of adventitious carbon to 284.6 eV. All of the XPS peaks were well deconvoluted and fitted by utilizing the Gaussian fitting method in Avantage program. Potentiostat/Galvanostat (VMP3, Bio-Logic) was used to implement the rotating disc electrode three electrode test and zinc air batteries cell performance evaluation.

2.3. Electrochemical Measurements. The three-electrode half-cell evaluation of materials was conducted by using rotating disc electrode (RDE) system (pine Inc.) at room temperature. In the three-electrode RDE system, the glassy carbon RDE electrode with the diameter of 5 mm as a working electrode, platinum wire electrode as a counter electrode, and Hg/HgO electrode as a reference electrode were used to conduct electrochemical measurement. The measured potential was corrected with respect to the reversible hydrogen electrode (RHE) based on the Nernst equation ($E_{\mathrm{RHE}} = E_{Hg/HgO}\,(0.118\ V) + 0.059 \times \mathrm{pH}\,13$, at 25°C and 1 atm). The linear sweep voltammetry (LSV) curves were measured using RDE system at a sweep rate of 5 mV s^{-1}, and the cyclic voltammetry (CV) curves are measured at a sweep rate of 20 mV s^{-1}. The catalyst ink for RDE test was composed of 10 mg of catalyst, 0.54 ml of DI water, 1.34 ml of ethanol, and 0.12 ml of Nafion solution (5 wt%, Sigma-Aldrich), and it was sonicated during 30 min before casting. The 8 μL of catalyst ink was casted on the surface of glassy carbon electrode, and its catalyst loading level was 37 $\mu g\,cm^{-2}$. For the OER and ORR measurement, O_2 (99.999%) was purged in 0.1 M KOH aqueous solution for 30 min before conducting measurement, and slight purging was maintained during the measurement. The CV at a scan rate of 500 mV s^{-1} was implemented before measurement for the stabilization of casted electrode in the electrolyte. The LSV curves of ORR were measured at a various rotating speed from 400 to 1600 rpm. The Koutechy-Levich (K-L) equation was used to determine the electron transfer number (n) of ORR.

$$\frac{1}{j} = \frac{1}{j_k} + \frac{1}{j_d} = \frac{1}{nFAkC_{O_2}} - \frac{1}{0.62nF\mathrm{AD}_{O_2}^{2/3}w^{1/2}}, \quad (1)$$

where j is the measured current density (A cm^{-2}), j_k is the kinetic current density (A cm^{-2}), j_d is the diffusion limiting current density (A cm^{-2}), F is the Faraday's constant (96485 C mol^{-1}), A is the geometric electrode surface area (cm^2), k is rate constant of the reaction, C_{O_2} is the bulk concentration of O_2 in 0.1 M KOH at 1 atm O_2 pressure (1.26×10^{-6} mol cm^{-3}), D_{O_2} is diffusion coefficient of O_2 (1.9×10^{-6} $cm^2\,s^{-1}$), ν is the kinematic viscosity of the electrolyte, 0.1 M KOH (1.09×10^{-2} $cm^2\,s^{-1}$), and ω is the angular velocity (rad s^{-1}).

2.4. Assembly and Test of RZAB Cells. The RZAB cells were utilized to evaluate the bifunctional electrocatalytic performance of the as-synthesized materials. The RZAB cell was composed of carbon cloth casted with catalyst as a cathode, Zn plate (Alfa Aesar) undergoing polishing as an anode, glassy fiber filter as a separator, and 6 M KOH with 0.2 M $Zn(ac)_2$ as an electrolyte. The catalyst ink for RZAB was composed of 14 mg of catalyst material, 0.15 ml DI water, 0.25 ml of Ethanol, and 0.18 ml of Nafion solution (5 wt%, Sigma-Aldrich) and sonicated for 30 min before casting on Teflon treated carbon cloth (W1S1009, Fuel Cell Store). After sonication, the catalyst ink was casted on the carbon cloth by brushing several times and dried under 80°C for 3 h in convection oven. The mass loading of air cathode for RZAB was about 2.9~3.0 mg cm^{-2}. RZAB cell test was conducted by using Bio-Logic instrument without gas flow.

3. Results and Discussion

The in situ growth of NiCoCr LDH on N-rGO is carried out through a simple hydrothermal synthesis method (Figure S1). The hierarchical structure of the as-synthesized NiCoCr LDH/N-rGO is constructed through the assembly of LDH nanosheets with tens of nm thickness grown onto the surface of N-rGO sheets as shown in Figures 1(a)–1(c). During the growth of LDHs on N-rGO, the nitrogen containing and oxygen terminating groups of N-rGO contributed to anchoring transition metal cations through the electrostatic interaction, which promotes nucleation and growth of LDHs. Therefore, NiCoCr LDH nanosheets were well grown on the N-rGO sheets, and the Ni, Co, and Cr transition metals were uniformly distributed onto the N-rGO, as indicated by the elemental mapping of Figures 1(d)–1(i). In addition, elemental mapping reveals that the N dopants are well distributed onto the rGO sheets, indicating uniform doping of N atoms. As shown in the TEM image of NiCoCr LDH/N-rGO in Figure 1(j), the NiCoCr LDH nanosheets with the average thickness of 30 nm were in-situ grown and well crystallized onto the N-rGO sheets with a lattice fringe spacing of 0.45 nm, which corresponds to (006) lattice plane of LDH (Figure 1(k)) [12]. As displayed in the above microscopic images, the NiCoCr LDH was successfully grown on the N-rGO nanosheets. The morphology of NiCoCr LDH looks like nanosheet on the N-rGO sheets with vertical and horizontal modes. This hierarchical structure can facilitate the mass transport of reactants and products of OER and ORR, which would be helpful for electrocatalytic reactions.

The XRD patterns of NiCoCr/N-rGO, NiCoCr LDH, NiCo LDH/N-rGO, and NiCo LDH are shown in Figure 2(a). The characteristic diffraction peaks of NiCo LDH and NiCo LDH/N-rGO were observed at $2\theta = 10.9^\circ$, 22.9°, 34.5°, 59.8°, and 61.2°, which correspond to (003), (006), (012), (110), and (113) of crystalline planes, respectively, for R3m symmetry of hydrotalcite phase (JCPDS#38-0715) [13, 14]. Even though Cr was introduced into the NiCo LDH, those peaks were observed for NiCoCr LDH, which implies that the hydrotalcite phase of LDH remains intact. After the growth of NiCoCr LDH on N-rGO sheets, most of these peaks were also preserved for NiCoCr LDH/N-rGO. Some peaks of pristine LDH in NiCoCr LDH/N-rGO disappeared due to the preferred growth direction during the in situ growth of LDH onto N-rGO. The basal spacing of NiCoCr LDH/N-rGO became larger than that of the pure NiCoCr LDH, as evidenced by the slight peak shift of (003) from $2\theta = 10.9^\circ$ to a lower angle of 10.8°, in the magnification of the (003) diffraction peak (Figure S2). The enlarged interlayer spacing is attributed to weakened electrostatic interactions between the LDH layers and interlayer species confined in interlayer space, which is presumably associated with the

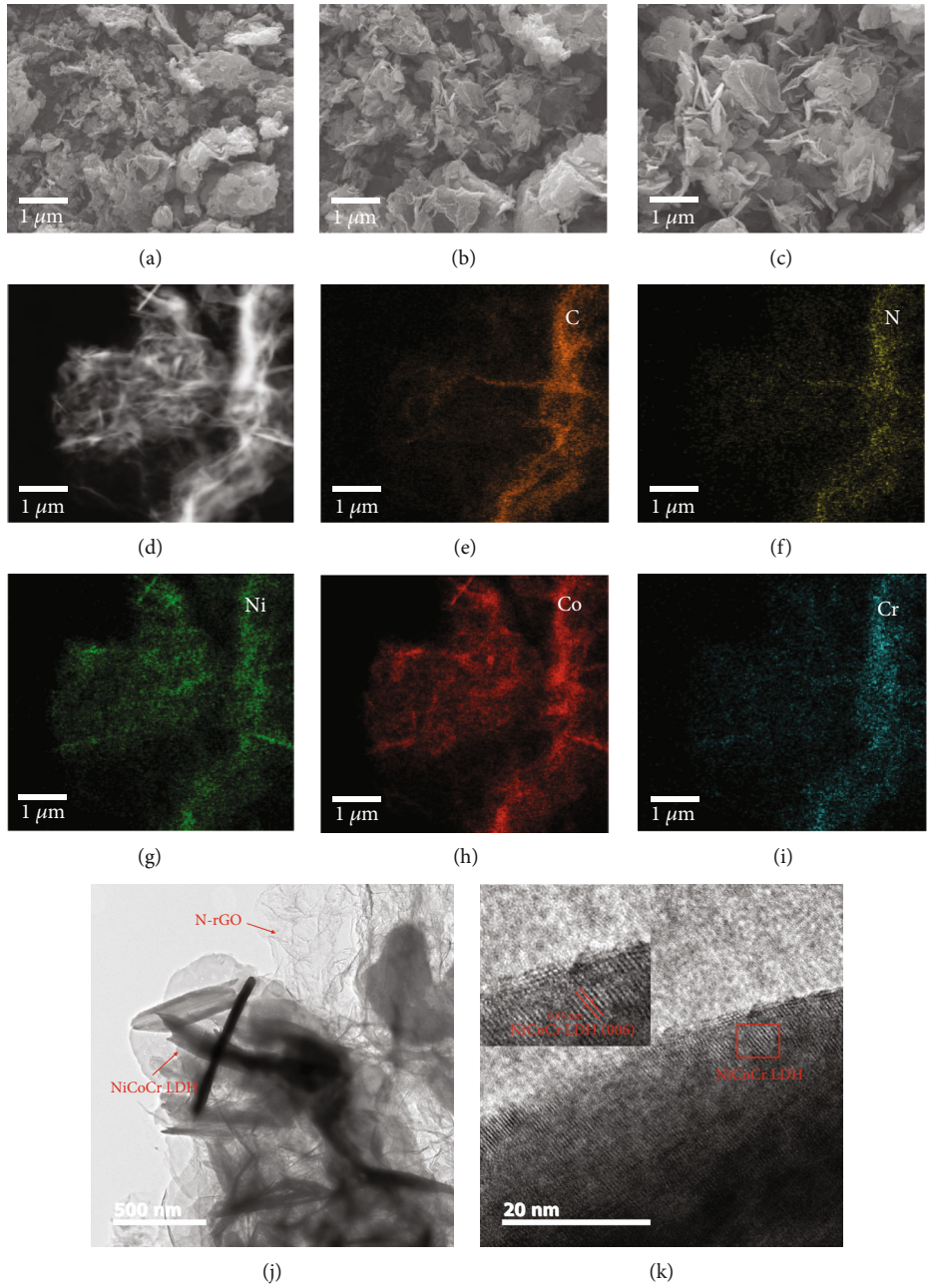

FIGURE 1: (a–c) FE-SEM images, (d) dark field TEM image, (e–i) corresponding elemental mapping images of C, N, Ni, Co, and Cr, (j) TEM image, and (k) HR-TEM image of NiCoCr LDH/N-rGO.

driving force for in situ growth of LDHs onto N-rGO sheets [15]. The broadened interlayer spacing is expected to facilitate the wetting and adsorption of OH^- onto the catalyst surface and to suppress the agglomeration of LDHs, which acts as ion buffering reservoirs of promoting ion transport and provides abundant active sites for the oxygen electrocatalytic reaction [16, 17].

The electronic structures of NiCoCr LDH/N-rGO, NiCo LDH/N-rGO, and N-rGO are characterized using the Raman spectra in Figure 2(b). These spectra exhibit two characteristic bands at 1358 and 1590 cm^{-1}, which correspond to the sp^3 defect sites of C atoms (D band) and the stretching vibration of sp^2 bonded atoms (G band), respectively [18]. The I_D/I_G ratios were estimated to compare the degree of defects in the graphene sheets. The I_D/I_G value of NiCoCr LDH/N-rGO is 1.13, which is slightly higher than 1.06 and 1.09 of pristine N-rGO and NiCo LDH/N-rGO, due to the formation of defects by Cr doping as further supported by XRD, TEM, and BET results [19]. These structural defects of NiCoCr LDH/N-rGO are attributed to more active sites for the improved electrocatalytic activity [20].

The N_2-adsorption/desorption measurements were conducted to understand the porous structure of NiCoCr LDH/N-rGO. The BET surface area of NiCoCr LDH/N-rGO is 40.34 $m^2 g^{-1}$, larger than 31.57 $m^2 g^{-1}$ of NiCo LDH/N-rGO as depicted in Figure 2(c) [21]. Additionally, the portion of

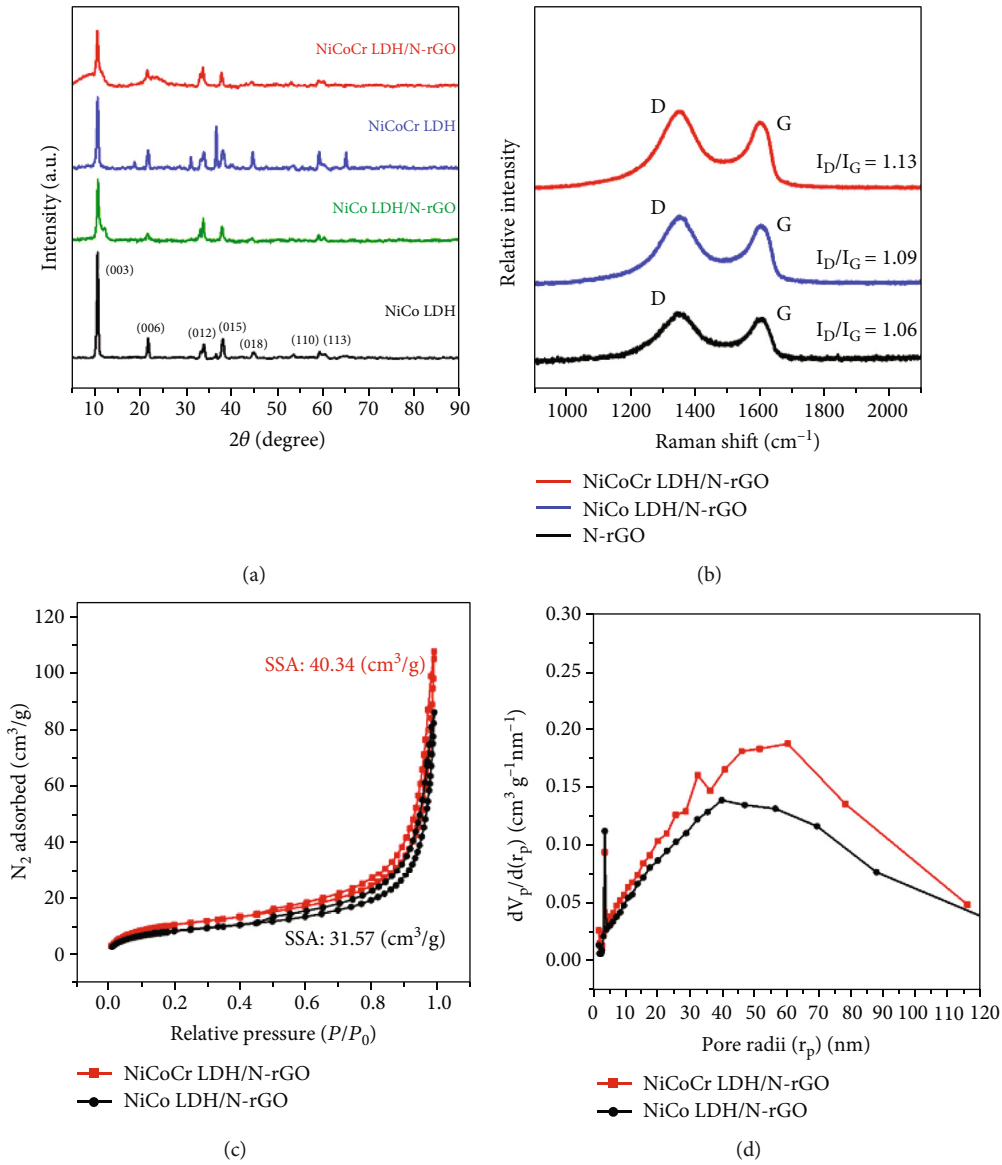

Figure 2: (a) XRD pattern of NiCoCr LDH/N-rGO, NiCoCr LDH, NiCo LDH/N-rGO, and NiCo LDH. (b) Raman spectra of NiCoCr LDH/N-rGO, NiCo LDH/N-rGO, and N-rGO. (c) N_2 adsorption and desorption isotherms of NiCoCr LDH/N-rGO and NiCo LDH/N-rGO, and (d) calculated pore size distributions of NiCoCr LDH/N-rGO and NiCo LDH/N-rGO.

mesopores with the size of 20 nm was increased after Cr doping into NiCo LDH/N-rGO as indicated by the BJH method in Figure 2(d) (Figure S3). Furthermore, the incorporation of Cr with smaller ionic radius could induce lattice distortion in the LDH layers, which is associated with the enlarged surface area of NiCo LDH/N-rGO. These surface area and mesoporosity of NiCoCr LDH/N-rGO were associated with the enlarged basal spacing of LDH and defect generation on N-rGO sheets, as demonstrated by the above XRD and the Raman spectra and TEM results [17]. Consequently, the increased surface area and mesoporosity arising from Cr doping can offer abundant active sites and rapid ion transport channels for the improved electrocatalytic performance [22].

XPS was tested to investigate the chemical and electronic structure of NiCoCr LDH/N-rGO, and the wide scan spectrum of NiCoCr LDH/N-rGO is shown in Figure S5A. As shown in Figure 3(a), the high-resolution Ni 2p XPS spectrum of NiCoCr LDH/N-rGO exhibits two oxidation states of Ni^{2+} at 855.1 and 872.6 eV and Ni^{3+} at 856.4 and 874.1 eV, respectively as well as shakeup satellite peaks at 862.4 and 880.4 eV [23]. The two oxidation states of Co in Co 2p XPS spectrum could be also observed at 782.3 and 797.7 eV for Co^{2+} and 780.5 and 796.2 eV for Co^{3+}, respectively (Figure 3(b)) [24–26]. An oxidation state of Cr^{3+} is existent in a form of Cr-OH (577.7 eV) and Cr-O (576.5 eV) from the high-resolution Cr 2p XPS spectrum (Figure 3(c)) [27]. As shown in the high-resolution N 1 s XPS spectrum (Figure 3(d)), three types of N species are assigned to pyridinic N, pyrrolic N, and graphitic N at 398.7, 399.6, and 400.6 eV, respectively [28]. Finally, four types of O species in the high-resolution O 1 s spectrum

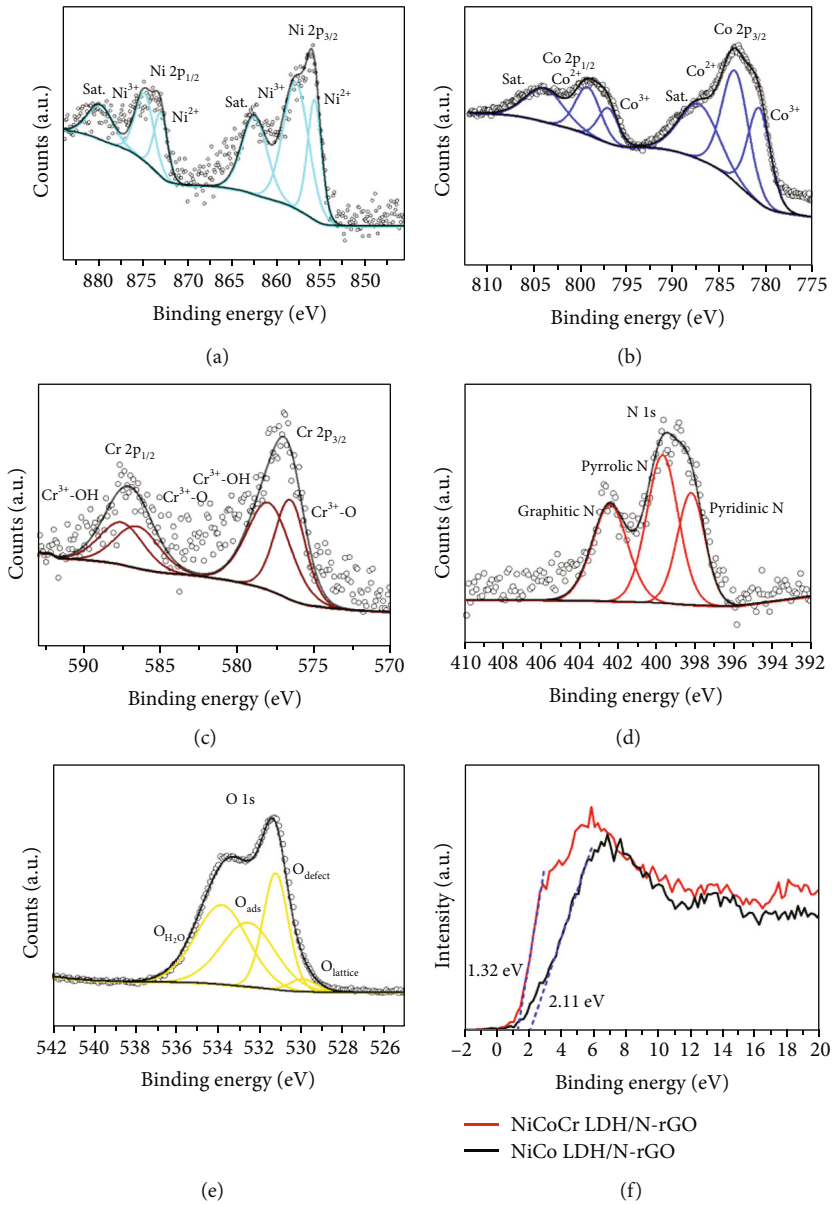

FIGURE 3: XPS spectra of (a) Ni 2p of NiCoCr LDH/N-rGO, (b) Co 2p of NiCoCr LDH/N-rGO, (c) Cr 2p spectrum of NiCoCr LDH/N-rGO, (d) N 1 s spectrum of NiCoCr LDH/N-rGO, (e) O 1 s spectrum of NiCoCr LDH/N-rGO, and (f) valence band maximum spectra of NiCoCr LDH/N-rGO and NiCo LDH/N-rGO.

are ascribed to O_{H2O}, O_{ads}, O_{defect}, and $O_{lattice}$ at 533.8, 532.5 531, and 529.6 eV, respectively (Figure 3(e)) [29]. Additionally, the high resolution XPS spectra of Ni (Figure S6A), Co (Figure S6B), N (Figure S6C), O (Figure S6D), and C (Figure S6E) are shown in Figure S6. Considering that the electron occupancy of e_g orbitals is a descriptor of the OER performance for transition metal electrocatalysts, a transition metal cation with an electron occupancy of e_g close to unity can achieve a superior OER performance [30]. The ratio of Co^{3+} ($t_{2g}^5e_g^1$) to Co^{2+} ($t_{2g}^5e_g^2$) increased after doping with Cr; hence, this strategy could be effective for enhancing OER catalytic activity. Accordingly, the increased Co^{3+} portion of NiCoCr LDH/N-rGO allows OER catalytic activity to be higher than that of NiCo LDH/N-rGO (Figure 3(b) and S6B) [31] The negative shift in binding energy of transition metal, after depositing the NiCoCr LDH onto the N-rGO sheets, indicates the modulation of electron density through a strong electronic interaction (Figure S4) [32]. In particular, the oxygen defects of NiCoCr LDH/N-rGO are attributed to the enhanced OER activity, lowering the energy barrier for the adsorption of OH^- toward a more kinetically favourable reaction pathway [33]. Additionally, C 1 s spectra support the increased oxygen defects via Cr doping (Figure S5B and S6E). In addition to the increased Co^{3+}, the portion of O_{defect} also increased after doping with Cr, such that, the OER catalytic activity is improved (Figure 3(e) and S6D) [34].

To further investigate the effect of Cr doping on the electronic structure of NiCoCr LDH/N-rGO, the valence band maximum spectra were collected for NiCoCr LDH/N-rGO and NiCo LDH/N-rGO, as shown in Figure 3(f). The valence band maximum level of NiCoCr LDH/N-rGO was higher than that of NiCo LDH/N-rGO, thus indicating that the bandgap energy was reduced after Cr doping. This reduced band gap of NiCoCr LDH/N-rGO, arising from the modulated electronic structure, can improve the electronic conduction for the enhanced catalytic activity [19]. For the further confirmation of enhanced conductivity after Cr doping, the powder resistivity measurement was conducted using 4 pin probe measurement (Figure S7). The electrical conductivity of NiCoCr LDH/N-rGO was higher than the sample without Cr, which is consistent with previous valence band maximum spectra results (Figure 3(f)).

The ORR performance of the NiCoCr LDH/N-rGO was measured in N_2 and O_2 saturated 0.1 M KOH electrolyte and compared with those of the NiCoCr LDH and Pt/C+RuO_2 as the reference (Figures S8). The current response of the NiCoCr LDH in CV curve is negligible under N_2 condition due to its low electronic conductivity and electrochemical active area. Even under O_2 condition, the ORR activity of the NiCoCr LDH was much lower than those of NiCoCr LDH/N-rGO and Pt/C+RuO_2. For the case of NiCoCr LDH/N-rGO, the capacitive behavior was presented in N_2 purged electrolyte, which indicates no side reactions in the electrochemical window of ORR (0.2–1.0 V vs. RHE). In the CV curve, there was an obvious oxygen reduction peak of the NiCoCr LDH/N-rGO in the O_2 purged electrolyte, which indicates an enhanced oxygen reduction activity by means of the composite with N-rGO with ORR activity [35].

The electrocatalytic activity of the as-prepared materials was evaluated in a three-electrode system using a rotating disk electrode (RDE) in a 0.1 M KOH solution. As shown in the LSV of NiCoCr LDH/N-rGO, NiCoCr LDH, NiCo LDH, N-rGO, and Pt/C+RuO_2 measured at a rotating speed of 1600 rpm, the half-wave potential ($E_{1/2}$) of NiCoCr LDH/N-rGO is 0.77 V, higher than those of NiCoCr LDH (0.51 V) and N-rGO (0.68 V) (Figure 4(a)). The superior ORR activity of NiCoCr LDH/N-rGO was further confirmed demonstrating the lowest Tafel slope of 37 mV/dec among the samples (Figure 4(c)). Moreover, the limiting current density of NiCoCr LDH/N-rGO is 4.9 mA/cm^2, higher than those of other samples except for Pt/C+RuO_2. The ORR activity of NiCoCr LDH/N-rGO was further analyzed obtaining the electron transfer number (n) for the ORR reaction from the Koutechy–Levich equation (K–L equation) based on the LSV curves at various rotating rates from 400 to 1600 rpm (Figure S9) [36]. In this work, the average electron transfer number at 0.5 V was 3.87, which is close to four indicating an ideal value for ORR catalytic pathway. These improved ORR activity and fast mass transport of NiCoCr LDH/N-rGO are attributed to the doping of Cr and hierarchical structure [37].

The OER performance of NiCoCr LDH/N-rGO was also evaluated in a 0.1 M KOH solution at a rotating rate of 1600 rpm (Figure 4(a)). The overpotential of NiCoCr LDH/N-rGO at a current density of 10 mA/cm^2 ($\Delta\eta_{j=10}$), which is an indicator for the evaluation of OER activity, was 340 mV, lower than those of the others except for 330 mV of NiCoCr LDH. Similarly, the Tafel slope of NiCoCr LDH/N-rGO for the OER is 62 mV/dec, lower than that of the others and slightly higher than 58 mV of NiCoCr LDH (Figure 4(d)) [38]. These results can be explained by increased defects of NiCo LDH by Co doping, such as oxygen defects, as indicated by the XPS results [39].

In order to evaluate bifunctional activity of NiCoCr LDH/N-rGO, its composition was optimized controlling the mass ratios from 1.5 : 1 to 4.5 : 1 in a 0.1 M KOH solution (Figure S10). The LDH/N-rGO-3.5 sample has the smallest total overpotential for the OER and ORR among all the samples. Accordingly, we evaluated the bifunctional activity using NiCoCr LDH/N-rGO-3.5 sample. The potential gaps between $E_{j=10}$ and $E_{1/2}$ of the electrocatalysts were compared in Figures 4(a) and 4(b). NiCoCr LDH/N-rGO exhibits the lower value of 0.8 V than those of NiCoCr LDH (1.04 V), NiCo LDH (1.18 V), and N-rGO (1.08 V), and even comparable to that of Pt/C+RuO_2 (0.8 V).

In order to clarify the effect of Cr doping on bifunctional catalytic activity, the ORR and OER electrocatalytic performances of NiCoCr LDH/N-rGO were measured using RDE and compared with NiCo LDH/N-rGO, and Pt/C+RuO_2 (Figures 4(f) and 4(h)). Based on the above results, with Cr doping, the electrocatalytic performance for both the OER and ORR was improved primarily from the perspective of the kinetics of the electrochemical reaction. As shown in Figure 4(f), the redox peak about 1.33 V is ascribed to the oxidation of $Ni(OH)_2$ to NiOOH during OER. During this process, the surface reconstruction occurs in NiCoCr LDH/N-rGO, where oxyhydroxide is formed onto the surface layer, as confirmed by the Raman spectra of NiCoCr LDH/N-rGO after OER in Figure S11C [40]. Furthermore, the dissolution of Cr occurs during OER, as demonstrated by the inset EDS results of Figures S11A and S11B. The surface reconstruction and Cr dissolution have the positive effects on porosity and active site, thereby enhancing electrocatalytic performances [41]. In order to confirm these effects, the turnover frequency (TOF) values of NiCoCr LDH/N-rGO, NiCo LDH/N-rGO, and Pt/C+RuO_2 are calculated using SEM EDX results in Table S2. The TOF value increased after Cr doping, originating from increased porosity and active sites of transition metal by the Cr doping (Table S1). The diffusion-limiting current density in the ORR increased with Cr doping, as illustrated in Figure 4(h), thus indicating enhanced mass transport for the reaction due to the increased mesopore in LDHs and also N-rGO. On the other hand, the Tafel slope of the OER is reduced with Cr doping, as shown in Figure 4(g), thus indicating facile kinetics originated from increased active sites and enhanced electrical conductivity. In particular, the enhancement of OER, and ORR performances due to Cr doping and hierarchical structure was further investigated estimating the electrochemical active surface area (ECSA) in Figure S12. The ECSA value increased after Cr doping, comparing NiCoCr LDH/N-rGO with NiCo LDH/N-rGO. When the Cr is introduced into the NiCo LDH/N-rGO, the specific

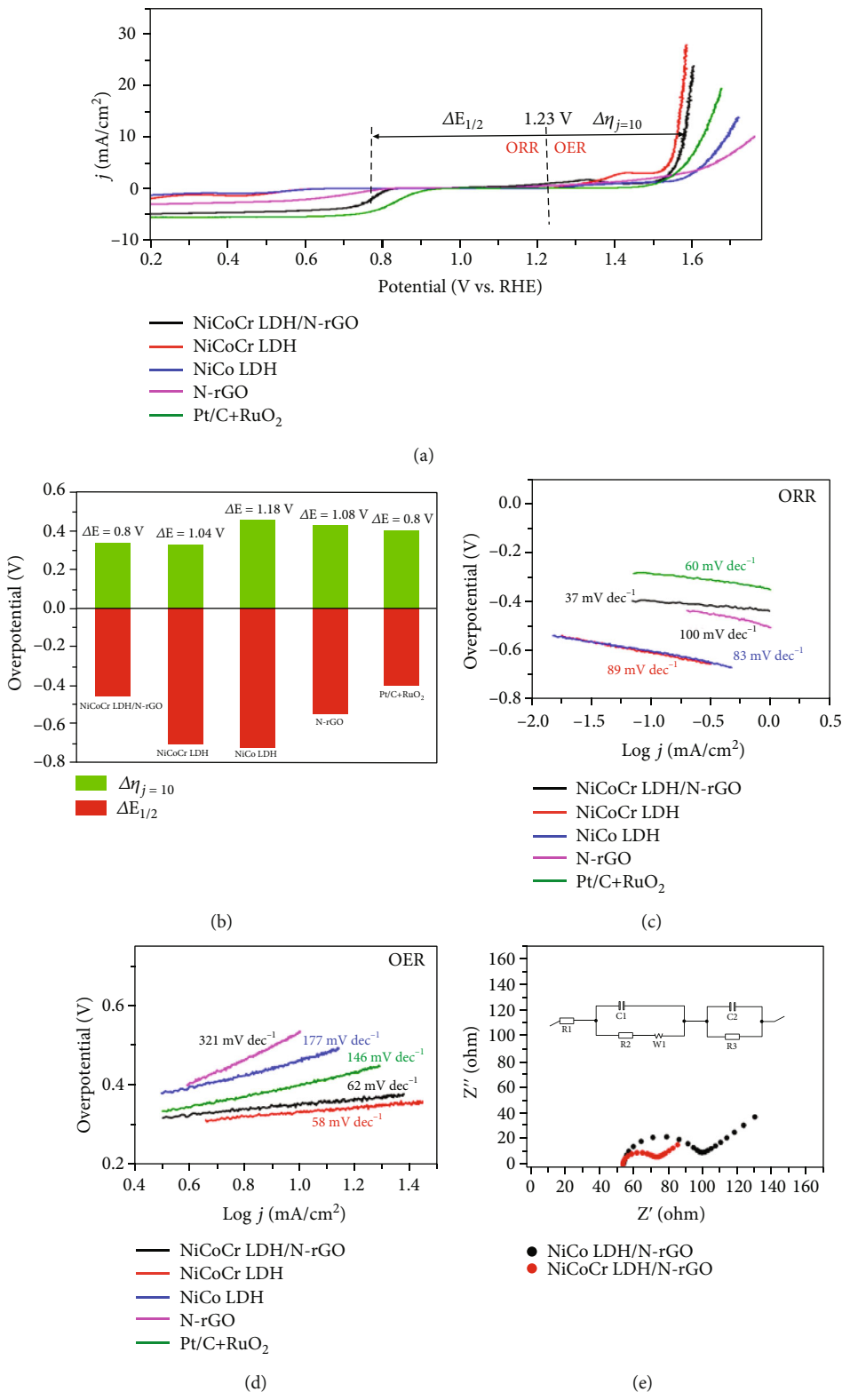

Figure 4: Continued.

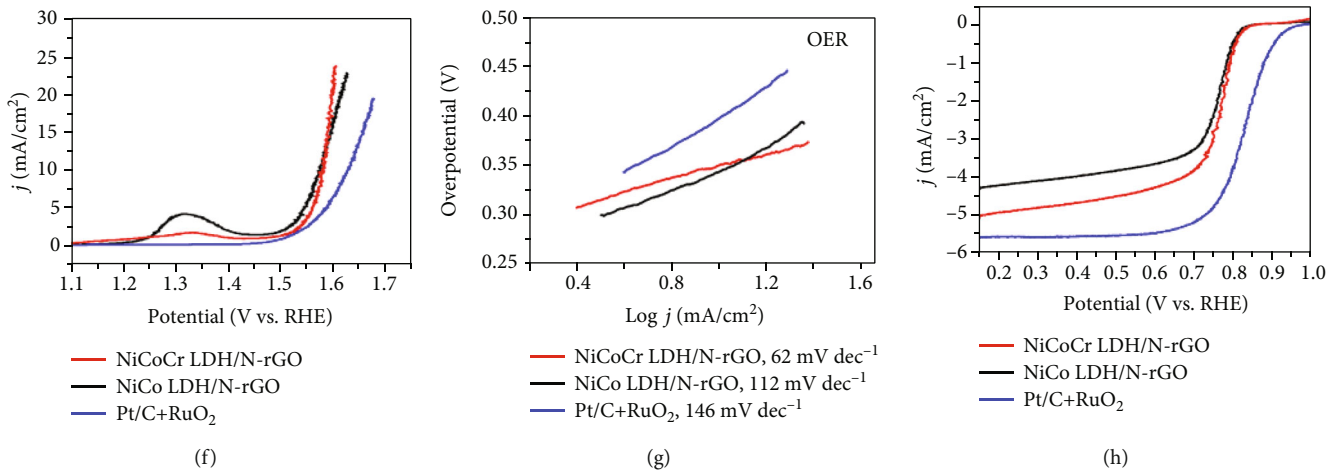

FIGURE 4: (a) LSVs of 1600 rpm of NiCoCr LDH/N-rGO, NiCoCr LDH, NiCo LDH, N-rGO, and Pt/C+RuO_2 in O_2 saturated 0.1 M KOH at 5 mV s^{-1}. (b) Corresponding total overpotential derived from LSV cures. (c) Corresponding Tafel's plot of ORR. (d) Corresponding Tafel's plot of OER. (e) Nyquist plot with a fitted equivalent circuit (inset) of NiCoCr LDH/N-rGO and NiCo LDH/N-rGO at 0.705 V (vs. Hg/HgO) measured from EIS. (f) OER LSVs of 1600 rpm of NiCoCr LDH/N-rGO, NiCo LDH/N-rGO, and Pt/C+RuO_2 in O_2 saturated 0.1 M KOH at 5 mV s^{-1}. (g) Corresponding Tafel's plot of OER. (h) ORR LSVs of 1600 rpm of NiCoCr LDH/N-rGO, NiCo LDH/N-rGO, and Pt/C+RuO_2 in O_2 saturated 0.1 M KOH at 5 mV s^{-1}.

surface area and mesoporosity are improved, and more defects in N-rGO are generated, as demonstrated by the BET, BJH, and the Raman spectra results (Figures 2(b)–2(d)). As derived from the surface electronic structure, the portion of Co3+ in Co species and the oxygen vacancy increased after Cr doping as shown in the Co 2p and O 1 s XPS spectra of NiCoCr LDH/N-rGO and NiCo LDH/N-rGO, indicating the increased number of active sites for OER (Figure 3). Moreover, the interlayer spacing in LDH structure is enlarged upon Cr doping (Figure S2), which could facilitate the wetting and adsorption of OH^- on the catalyst surface and offer easy access to active sites for oxygen electrocatalytic reaction. These results indicate more accessible active sites for the improved OER and ORR performances. Therefore, the increased OER and ORR catalytic activity due to Cr doping is ascribed to the increased porosity, defects, and structural disorders in the material, such as oxygen defects and structural imperfections in the LDHs and N-rGO sheets, which play a considerable role of enhancing the catalytic activity for the OER and ORR [42, 43]. Eventually, Cr doping is an effective method to further enhance the electrocatalytic performance of RZABs. Based on these results, NiCoCr LDH/N-rGO achieved sufficient bifunctional activity owing to the introduction of Cr dopants and N-rGO substrates, which is comparable to commercial precious metal-based catalysts.

Moreover, Nyquist plots fitted with the equivalent circuit model of NiCoCr LDH/N-rGO and NiCo LDH/N-rGO are depicted in Figure 4(e) [44]. Based on the above results, the semicircle diameter of NiCoCr LDH/N-rGO in the high-frequency region indicates that the charge transfer resistance of the reaction is lower than that of NiCo LDH/N-rGO [45]. Essentially, it implies that more facile charge transfer occurs at the interface owing to the lower charge transfer resistance originating from Cr doping. The reduced charge transfer resistance is related to the increased electrical conductivity originating from the reduced bandgap energy after doping with Cr. Accordingly, the facile reaction kinetics of the OER and ORR of NiCoCr LDH/N-rGO were ascribed to the Cr doping, increased electrical conductivity, large surface area, and mesoporosity in both LDHs and N-rGO, which could help promote charge transfer and mass transport kinetics in the reaction. Furthermore, the overall electrocatalytic activity for OER and ORR of NiCoCr LDH/N-rGO was compared with performance of previous reported electrocatalysts, and the results demonstrate that the NiCoCr LDH/N-rGO has superior electrocatalytic performance for OER and ORR compared to other reports because of Cr doping and hierarchical structure (Table S3).

Based on the above evaluation of the electrocatalytic performance for the OER and ORR, NiCoCr LDH/N-rGO could be applied for the bifunctional electrocatalyst of the RZAB, which uses oxygen evolution and reduction reactions during charging and discharging, respectively. For the RZAB test, a homemade RZAB was assembled, using zinc foil as the anode, NiCoCr LDH/N-rGO as the air cathode, glass fiber membrane as the separator, and 6 M KOH with 0.2 M Zn acetate as the electrolyte [46]. Among NiCoCr LDH/N-rGO samples, LDH/N-rGO-3.5 was chosen as a bifunctional electrocatalyst for RZAB, and, for the counter sample, the Pt/C+RuO_2 was used.

In Figure 5(a), the open-circuit voltage (OCV) of NiCoCr LDH/N-rGO is shown as 1.38 V, which is comparable to that of Pt/C+RuO_2 [47]. The charging and discharging polarization curves of NiCoCr LDH/N-rGO and Pt/C+RuO_2 are depicted in Figure 5(b). The overpotential for the charging and discharging of NiCoCr LDH/N-rGO was lower than that of Pt/C +RuO_2, particularly at a high current density. The specific capacities of RZABs with the NiCoCr LDH/N-rGO and Pt/C +RuO_2 were calculated on a basis of the mass of Zn. The RZAB with the NiCoCr LDH/N-rGO achieved the higher specific

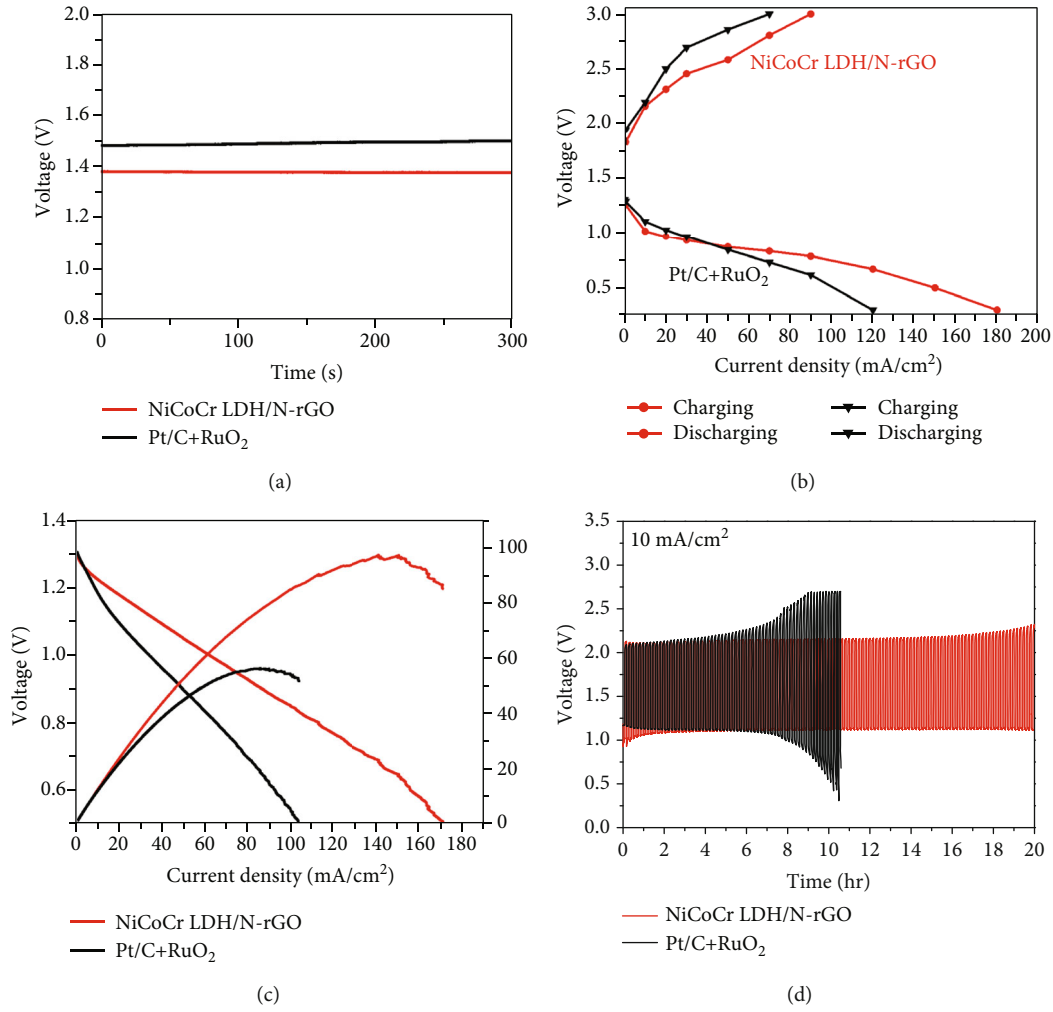

Figure 5: (a) Open circuit potential of Zinc air batteries of NiCoCr LDH/N-rGO and Pt/C+RuO_2; (b) charging and discharging polarization curves of NiCoCr LDH/N-rGO and Pt/C+RuO_2; (c) discharge polarization curve and corresponding power density of Zinc air batteries using NiCoCr LDH/N-rGO and Pt/C+RuO_2; (d) charging and discharging cycling curves of Zinc air batteries using NiCoCr LDH/N-rGO and Pt/C+RuO_2.

capacity of 559 mAh g^{-1}_{Zn} than 462 mAh g^{-1}_{Zn} with Pt/C +RuO_2 shown in Figure S13, which is beneficial for high energy density [48]. In addition, the power density of NiCoCr LDH/N-rGO was much higher than that of Pt/C+RuO_2, as shown in Figure 5(c), which indicates the superior kinetics of NiCoCr LDH/N-rGO as a bifunctional electrocatalyst for RZAB. The overall cell resistance was reduced, which is attributed to the electrocatalytic activity and facile adsorption/desorption of the reactant/product during the reaction.

The cycle stability of the RZAB was evaluated using NiCoCr LDH/N-rGO and Pt/C+RuO_2 as counter samples at a current density of 10 mA/cm^2 with a cycling rate of 20 min per cycle. As shown in Figure 5(d), the overpotential between charging and discharging was higher for NiCoCr/N-rGO than for Pt/C+RuO_2 during the initial cycling because of the activation of the electrochemical reaction [49]. After the activation cycles, the voltage plateau of charging and discharging was 2.05 V and 1.1 V for NiCoCr LDH/N-rGO and 2.1 V and 1.1 V for Pt/C+RuO_2, and the overpotential between charging and discharging for NiCoCr LDH/N-rGO became lower than Pt/C+RuO_2. After 60 cycles, the voltage gap between charging and discharging exhibited no significant change in NiCoCr LDH/N-rGO; it exhibited a stable voltage plateau until 100 cycles. However, the voltage gap of Pt/C+RuO_2 became much larger than that of the initial state. These results indicate that the cycling stability of NiCoCr LDH/N-rGO was superior to that of Pt/C+RuO_2. The reason for superior stability of NiCoCr LDH/N-rGO was ascribed to its stability in an alkaline electrolyte [50]. Pt-like noble metals loaded on carbon have poor stability in alkaline electrolytes because of their degradation mechanism derived from carbonate production and nanoparticle detachment [51]. In contrast to noble metal-based electrocatalysts, NiCoCr LDH was grown on N-rGO nanosheets and chemically bonded to each other to avoid particle aggregation and detachment from the conductive supports [52]. Thus, NiCoCr LDHN-rGO is a suitable bifunctional electrocatalysts for RZAB.

In order to clarify the Cr doping effect on RZAB, NiCo LDH/N-rGO was applied as a bifunctional electrocatalyst for

RZAB under the same conditions as the above RZAB tests. In Figure S14A, the OCV of NiCoCr LDH/N-rGO and NiCo LDH/N-rGO were almost saturated to same value of 1.38 V, thus indicating that the dopant of Cr has a negligible effect on the OCV of RZAB. The charging and discharging polarization curves of NiCoCr LDH/N-rGO and NiCo LDH/N-rGO are depicted in Figure S14B. The overpotential between charging and discharging was much lower for NiCoCr LDH/N-rGO than for NiCo LDH/N-rGO, thus indicating that Cr is an effective dopant for LDH-based electrocatalysts in RZABs. The reduced polarization of the RZAB after Cr doping can be ascribed to the increased mass transport kinetics related to the increased surface area, porosity, and ion channels. The reactants and products could adsorb and desorb from the catalytic active sites and migrate easily when the Cr dopants were introduced in LDH/N-rGO; thus, the kinetics became more facile. In addition, the cycle stability of RZAB was evaluated using NiCoCr LDH/N-rGO and NiCo LDH/N-rGO as the counter sample at a current density of 10 mA/cm^2 with a cycling rate of 20 min per cycle. The results presented in Figure S14C indicate that Cr could effectively advance the stability of the bifunctional electrocatalyst for RZAB. The enhanced stability after doping with Cr could be ascribed to the enlarged interlayer spacing of LDHs and increased structural defects of N-rGO nanosheets because these effects could mitigate the aggregation among particles and graphene sheets, which could maintain the active sites accessible longer than the sample without Cr. Furthermore, Nyquist plots of NiCoCr LDH/N-rGO and NiCo LDH/N-rGO fitted with a randle circuit are presented in Figure S14D using RZAB. The charge-transfer resistance of NiCoCr LDH/N-rGO was smaller than that of NiCo LDH/N-rGO, which is consistent with the above RDE results. Therefore, Cr doping could be an effective way to enhance the catalytic performance of RZAB.

4. Conclusion

In this study, we have demonstrated NiCoCr LDH/N-rGO as a novel bifunctional electrocatalyst material for RZAB. The incorporation of Cr into LDH enhanced the OER and ORR performance of the electrocatalyst owing to the increased specific surface area and defect concentration. From evaluation of OER and ORR catalytic performance, the NiCoCr LDH/N-rGO exhibits an attractive performance of OER with $\Delta\eta_{j=10}$ of 340 mV for the performance descriptor of OER and $E_{1/2}$ of 0.77 V for that of ORR, such that the integrated overpotential of NiCoCr LDH/N-rGO is 0.8 V, which is smaller than NiCo LDH/N-rGO, NiCoCr LDH, NiCo LDH, N-rGO, and comparable to Pt/C+RuO_2. Additionally, the RZAB test was also conducted using NiCoCr LDH/N-rGO as a bifunctional electrocatalyst for air cathodes. NiCoCr LDH/N-rGO exhibited superior rate capability, power density (97 mW cm^{-2} for NiCoCr/N-rGO vs. 59 mW cm^{-2} for Pt/C+RuO_2), and stability (stable cycling during 18 h for NiCoCr LDH/N-rGO vs. 6 h for Pt/C+RuO_2) compared to Pt/C+RuO_2 and NiCo LDH/N-rGO because of its superior stability in alkaline electrolytes. Finally, the doping of Cr into LDH and composites with nitrogen-doped reduced graphene oxide can be considered an appropriate method for rendering the electrocatalytic performance affordable for RZAB based on LDH catalysts.

Data Availability

Data are available on request.

Conflicts of Interest

The authors declare that there is no competing financial interest.

Acknowledgments

This work was supported by R&D Program for Forest Science Technology (Project No. 2021354B10-2123-AC03) provided by the Korea Forest Service (Korea Forestry Promotion Institute), the Energy Efficiency and Resources Core Technology Program of the Korea Institute of Energy Technology Evaluation and Planning, financial grants from the Ministry of Trade, Industry & Energy, Republic of Korea (No. 20214910100070), and the Technology Innovation Program (20004958, development of ultrahigh performance supercapacitor and high power module) funded by the Ministry of Trade, Industry and Energy (MOTIE).

Supplementary Materials

Figure S1: schematic illustration of synthesizing process of NiCoCr LDH/N-rGO. Figure S2: magnification of (0 0 3) diffraction peak of XRD pattern of NiCoCr LDH/N-rGO and NiCoCr LDH. Figure S3: TEM images of (A) NiCo LDH/N-rGO; (B)-(C) NiCoCr LDH/N-rGO. Figure S4: high resolutions Co 2p spectra of NiCoCr LDH/N-rGO and NiCoCr LDH. Figure S5: (A) XPS wide scan of NiCoCr LDH/N-rGO. (B) High resolutions C 1 s spectra of NiCoCr LDH/N-rGO. Figure S6: XPS of high resolutions (A) Ni 2p; (B) Co 2p; (C) N 1 s; (D) O 1 s; (E) C 1 s spectra of NiCo LDH/N-rGO. Figure S7: powder resistivity measurement of NiCoCr LDH/N-rGO and NiCo LDH/N-rGO. Figure S8: CVs in N_2 and O_2 Saturated 0.1 M KOH for (A) Pt/C+RuO_2; (B) NiCoCr LDH; (C) NiCoCr LDH/N-rGO at 20 mV s^{-1}. Figure S9: (A) RDE voltammograms of NiCoCr LDH/N-rGO in O_2 saturated 0.1 M KOH at scan rate of 5 mV s^{-1}. (B) Corresponding K-L plot of NiCoCr LDH/N-rGO. Figure S10: (A) OER LSVs of 1600 rpm of different mass ratios of composites of NiCoCr LDH/N-rGO in O_2 saturated 0.1 M KOH at 5 mV s^{-1}. (B) Corresponding overpotential plot of OER. (C) ORR LSVs of 1600 rpm of different mass ratio of composites of NiCoCr LDH/N-rGO in O_2 saturated 0.1 M KOH at 5 mV s^{-1}. (D) Corresponding overpotential plot of ORR. Figure S11: FE-SEM images with EDS analysis (inset) of (A) NiCoCr LDH/N-rGO before OER; (B) NiCoCr LDH/N-rGO after OER 300 cycles in 0.1 M KOH at 5 mV s^{-1}; (C) Raman spectra of NiCoCr LDH/N-rGO before and after OER 300cycles in 0.1 M KOH at 5 mV s^{-1}. Figure S12: CV curves of NiCoCr LDH/N-rGO, NiCo LDH/N-rGO, physical mixing of NiCoCr LDH, and N-rGO in the nonfaradaic potential region at

different scan rates of 10, 20, 30, 40, and 50 mV s-1 for (A) NiCoCr LDH/N-rGO; (B) NiCo LDH/N-rGO; (C) physical mixing; (E) corresponding plot of average current density of anodic and catholic sweep at -0.65 V vs. SCE as a function of scan rate. Figure S13: plot of voltage vs. specific capacity (based on the mass of Zn plate) at 5 mA cm^{-2} of NiCoCr LDH/N-rGO and Pt/C+RuO_2. Figure S14: (A) open circuit potential of Zinc air batteries of NiCoCr LDH/N-rGO and NiCo LDH/N-rGO. (B) Charging and discharging polarization curves of NiCoCr LDH/N-rGO and NiCo LDH/N-rGO. (C) Charging and discharging cycling curves of Zinc air batteries using NiCoCr LDH/N-rGO and NiCo LDH/N-rGO. (D) Nyquist plots with a fitted equivalent circuit (inset) of Zinc air batteries using NiCoCr LDH/N-rGO and NiCo LDH/N-rGO. Table S1: calculation of turnover frequency (TOF) of NiCoCr LDH/N-rGO, NiCo LDH/N-rGO, and Pt/C+RuO_2. Table S2: SEM elemental distribution analysis (EDX) of NiCoCr LDH/N-rGO and NiCo LDH/N-rGO. Table S3: Comparison table of ORR and OER bifunctional electrocatalyst performance of reported transition metal compound and carbon composite-based electrocatalysts in 0.1 M KOH electrolyte. *(Supplementary Materials)*

References

[1] X. Chen, Z. Zhou, H. E. Karahan, Q. Shao, L. Wei, and Y. Chen, "Recent advances in materials and design of electrochemically rechargeable zinc–air batteries," *Small*, vol. 14, no. 44, article e1801929, 2018.

[2] J. Fu, R. Liang, G. Liu et al., "Recent progress in electrically rechargeable zinc–air batteries," *Advanced Materials*, vol. 31, article e1805230, 2019.

[3] E. Davari and D. Ivey, "Bifunctional electrocatalysts for Zn–air batteries," *Sustainable Energy & Fuels*, vol. 2, no. 1, pp. 39–67, 2018.

[4] H. F. Wang, C. Tang, and Q. Zhang, "A review of precious-metal-free bifunctional oxygen electrocatalysts: rational design and applications in Zn−air batteries," *Advanced Functional Materials*, vol. 28, no. 46, p. 1803329, 2018.

[5] S. Ren, X. Duan, S. Liang, M. Zhang, and H. Zheng, "Bifunctional electrocatalysts for Zn–air batteries: recent developments and future perspectives," *Journal of Materials Chemistry A*, vol. 8, no. 13, pp. 6144–6182, 2020.

[6] S. Anantharaj, K. Karthick, and S. Kundu, "Evolution of layered double hydroxides (LDH) as high performance water oxidation electrocatalysts: a review with insights on structure, activity and mechanism," *Materials Today Energy*, vol. 6, pp. 1–26, 2017.

[7] H. Yi, S. Liu, C. Lai et al., "Recent advance of transition-metal-based layered double hydroxide nanosheets: synthesis, properties, modification, and electrocatalytic applications," *Advanced Energy Materials*, vol. 11, no. 14, p. 2002863, 2021.

[8] F. Song and X. Hu, "Exfoliation of layered double hydroxides for enhanced oxygen evolution catalysis," *Nature Communications*, vol. 5, no. 1, pp. 1–9, 2014.

[9] T. Wang, J. Wu, Y. Liu et al., "Scalable preparation and stabilization of atomic-thick CoNi layered double hydroxide nanosheets for bifunctional oxygen electrocatalysis and rechargeable zinc-air batteries," *Energy Storage Materials*, vol. 16, pp. 24–30, 2019.

[10] L. Lai, J. R. Potts, D. Zhan et al., "Exploration of the active center structure of nitrogen-doped graphene-based catalysts for oxygen reduction reaction," *Energy & Environmental Science*, vol. 5, no. 7, pp. 7936–7942, 2012.

[11] G. Lee and J. Jang, "High-performance hybrid supercapacitors based on novel Co_3O_4/$Co(OH)_2$ hybrids synthesized with various-sized metal-organic framework templates," *Journal of Power Sources*, vol. 423, pp. 115–124, 2019.

[12] T. Li, R. Li, and H. Luo, "Facile in situ growth of Ni/Co-LDH arrays by hypothermal chemical coprecipitation for all-solid-state asymmetric supercapacitors," *Journal of Materials Chemistry A*, vol. 4, no. 48, pp. 18922–18930, 2016.

[13] X. Xue, J. Zhong, J. Liu et al., "Hydrolysis of metal-organic framework towards three-dimensional nickel cobalt- layered double hydroxide for high performance supercapacitors," *Journal of Energy Storage*, vol. 31, article 101649, 2020.

[14] Y. Li, L. Shan, Y. Sui et al., "Ultrathin Ni–Co LDH nanosheets grown on carbon fiber cloth via electrodeposition for high-performance supercapacitors," *Journal of Materials Science: Materials in Electronics*, vol. 30, no. 14, pp. 13360–13371, 2019.

[15] M. Li, J. Cheng, J. Wang, F. Liu, and X. Zhang, "The growth of nickel-manganese and cobalt-manganese layered double hydroxides on reduced graphene oxide for supercapacitor," *Electrochimica Acta*, vol. 206, pp. 108–115, 2016.

[16] L. Wang, Z. H. Dong, Z. G. Wang, F. X. Zhang, and J. Jin, "Layered α-Co(OH)2 nanocones as electrode materials for pseudocapacitors: understanding the effect of interlayer space on electrochemical activity," *Advanced Functional Materials*, vol. 23, no. 21, pp. 2758–2764, 2013.

[17] D. Zhou, Z. Cai, X. Lei et al., "NiCoFe-layered double hydroxides/N-doped graphene oxide array colloid composite as an efficient bifunctional catalyst for oxygen electrocatalytic reactions," *Advanced Energy Materials*, vol. 8, no. 9, p. 1701905, 2018.

[18] X. C. Li, W. J. An, and S. Kim, "Large-area synthesis of high-quality and uniform graphene films on copper foils," *Science*, vol. 324, no. 5932, pp. 1312–1314, 2009.

[19] T. H. Park, J. S. Yeon, P. Sivakumar, Y. Kim, and H. S. Park, "Bifunctional mesoporous CoO/nitrogen-incorporated graphene electrocatalysts for high-power and long-term stability of rechargeable zinc-air batteries," *International Journal of Energy Research*, vol. 45, no. 5, pp. 6698–6707, 2021.

[20] H. Xu, B. Wang, C. Shan, P. Xi, W. Liu, and Y. Tang, "Ce-doped NiFe-layered double hydroxide ultrathin nanosheets/nanocarbon hierarchical nanocomposite as an efficient oxygen evolution catalyst," *ACS Applied Materials & Interfaces*, vol. 10, no. 7, pp. 6336–6345, 2018.

[21] C. Ramirez-Barria, C. López-Olmos, A. Guerrero-Ruiz, and I. Rodríguez-Ramos, "Direct catalytic effect of nitrogen functional groups exposed on graphenic materials when acting cooperatively with Ru nanoparticles," *RSC Advances*, vol. 7, no. 70, pp. 44568–44577, 2017.

[22] B. Jiang, Y. Guo, J. Kim et al., "Mesoporous metallic iridium nanosheets," *Journal of the American Chemical Society*, vol. 140, no. 39, pp. 12434–12441, 2018.

[23] M. R. Kandel, U. N. Pan, D. R. Paudel, P. P. Dhakal, N. H. Kim, and J. H. Lee, "Hybridized bimetallic phosphides of Ni-Mo, Co-Mo, and Co-Ni in a single ultrathin-3D-nanosheets for efficient HER and OER in alkaline media," *Composites Part B: Engineering*, vol. 239, article 109992, 2022.

[24] J. Jiang, A. Zhang, L. Li, and L. Ai, "Nickel-cobalt layered double hydroxide nanosheets as high-performance electrocatalyst for oxygen evolution reaction," *Journal of Power Sources*, vol. 278, pp. 445–451, 2015.

[25] A. Muthurasu, A. P. Tiwari, K. Chhetri, B. Dahal, and H. Y. Kim, "Construction of iron doped cobalt- vanadate- cobalt oxide with metal-organic framework oriented nanoflakes for portable rechargeable zinc-air batteries powered total water splitting," *Nano Energy*, vol. 88, article 106238, 2021.

[26] K. Chhetri, A. Muthurasu, B. Dahal et al., "Engineering the abundant heterointerfaces of integrated bimetallic sulfide-coupled 2D MOF-derived mesoporous CoS_2 nanoarray hybrids for electrocatalytic water splitting," *Materials Today Nano*, vol. 17, article 100146, 2022.

[27] Y. Yang, L. Dang, M. J. Shearer et al., "Highly active trimetallic NiFeCr layered double hydroxide electrocatalysts for oxygen evolution reaction," *Advanced Energy Materials*, vol. 8, no. 15, article 1703189, 2018.

[28] T. Zhan, Y. Zhang, X. Liu, S. Lu, and W. Hou, "NiFe layered double hydroxide/reduced graphene oxide nanohybrid as an efficient bifunctional electrocatalyst for oxygen evolution and reduction reactions," *Journal of Power Sources*, vol. 333, pp. 53–60, 2016.

[29] Y. Wang, Q. Jiang, L. Xu et al., "Effect of the configuration of copper oxide–ceria catalysts in NO reduction with CO: superior performance of a copper–ceria solid solution," *ACS Applied Materials & Interfaces*, vol. 13, no. 51, pp. 61078–61087, 2021.

[30] J. Suntivich, K. J. May, H. A. Gasteiger, J. B. Goodenough, and Y. Shao-Horn, "A perovskite oxide optimized for oxygen evolution catalysis from molecular orbital principles," *Science*, vol. 334, no. 6061, pp. 1383–1385, 2011.

[31] J. Li, W. Xu, R. Li et al., "A tremella-like Ni76Co24 layered double hydroxides nanosheets as an efficient catalyst for oxygen evolution reaction," *Journal of Materials Science*, vol. 51, no. 20, pp. 9287–9295, 2016.

[32] S. Li, C. Yu, J. Yang et al., "A superhydrophilic "nanoglue" for stabilizing metal hydroxides onto carbon materials for high-energy and ultralong-life asymmetric supercapacitors," *Energy & Environmental Science*, vol. 10, no. 9, pp. 1958–1965, 2017.

[33] D. Zhou, X. Xiong, Z. Cai et al., "Flame-engraved nickel-iron layered double hydroxide nanosheets for boosting oxygen evolution reactivity," *Small Methods*, vol. 2, no. 7, article 1800083, 2018.

[34] J. Li, R. Lian, J. Wang, S. He, and Z. Rui, "Oxygen vacancy defects modulated electrocatalytic activity of iron-nickel layered double hydroxide on Ni foam as highly active electrodes for oxygen evolution reaction," *Electrochimica Acta*, vol. 331, article 135395, 2020.

[35] Y. Qian, T. An, E. Sarnello, Z. Liu, T. Li, and D. Zhao, "Janus electrocatalysts containing MOF-derived carbon networks and NiFe-LDH nanoplates for rechargeable zinc–air batteries," *ACS Applied Energy Materials*, vol. 2, no. 3, pp. 1784–1792, 2019.

[36] R. Zhou, Y. Zheng, M. Jaroniec, and S.-Z. Qiao, "Determination of the electron transfer number for the oxygen reduction reaction: from theory to experiment," *ACS Catalysis*, vol. 6, no. 7, pp. 4720–4728, 2016.

[37] W. Wang, Y. Liu, J. Li, J. Luo, L. Fu, and S. Chen, "NiFe LDH nanodots anchored on 3D macro/mesoporous carbon as a high-performance ORR/OER bifunctional electrocatalyst," *Journal of Materials Chemistry A*, vol. 6, no. 29, pp. 14299–14306, 2018.

[38] C. C. Gudal, U. N. Pan, D. R. Paudel, M. R. Kandel, N. H. Kim, and J. H. Lee, "Bifunctional P-intercalated and doped metallic (1T)-copper molybdenum sulfide ultrathin 2D-nanosheets with enlarged interlayers for efficient overall water splitting," *ACS Applied Materials & Interfaces*, vol. 14, no. 12, pp. 14492–14503, 2022.

[39] X. Zhang, Y. Zhao, Y. Zhao, R. Shi, G. I. N. Waterhouse, and T. Zhang, "A simple synthetic strategy toward defect-rich porous monolayer NiFe-layered double hydroxide nanosheets for efficient electrocatalytic water oxidation," *Advanced Energy Materials*, vol. 9, no. 24, article 1900881, 2019.

[40] J.-J. Zhang, M. Y. Li, W. W. Bao et al., "Cr-doped NiZn layered double hydroxides with surface reconstruction toward the enhanced water splitting," *Colloids and Surfaces A: Physicochemical and Engineering Aspects*, vol. 649, article 129324, 2022.

[41] D. Xu, M. B. Stevens, Y. Rui et al., "The role of Cr doping in NiFe oxide/(oxy) hydroxide electrocatalysts for oxygen evolution," *Electrochimica Acta*, vol. 265, pp. 10–18, 2018.

[42] P. Li, X. Duan, Y. Kuang et al., "Tuning electronic structure of NiFe layered double hydroxides with vanadium doping toward high efficient electrocatalytic water oxidation," *Advanced Energy Materials*, vol. 8, no. 15, article 1703341, 2018.

[43] C. Dong, X. Zhang, J. Xu et al., "Ruthenium-doped cobalt–chromium layered double hydroxides for enhancing oxygen evolution through regulating charge transfer," *Small*, vol. 16, no. 5, article 1905328, 2020.

[44] C. Ye, M.-Q. Wang, S.-J. Bao, and C. Ye, "Micropore-boosted layered double hydroxide catalysts: EIS analysis in structure and activity for effective oxygen evolution reactions," *ACS Applied Materials & Interfaces*, vol. 11, no. 34, pp. 30887–30893, 2019.

[45] S.-M. Ji, A. Muthurasu, K. Chhetri, and H. Y. Kim, "Metal-organic framework assisted vanadium oxide nanorods as efficient electrode materials for water oxidation," *Journal of Colloid and Interface Science*, vol. 618, pp. 475–482, 2022.

[46] X. Han, N. Li, P. Xiong et al., "Electronically coupled layered double hydroxide/MXene quantum dot metallic hybrids for high-performance flexible zinc–air batteries," *InfoMat*, vol. 3, no. 10, pp. 1134–1144, 2021.

[47] R. Zhao, Q. Li, Z. Chen et al., "B, N-doped ultrathin carbon nanosheet superstructure for high-performance oxygen reduction reaction in rechargeable zinc-air battery," *Carbon*, vol. 164, pp. 398–406, 2020.

[48] N. Logeshwaran, S. Ramakrishnan, S. S. Chandrasekaran et al., "An efficient and durable trifunctional electrocatalyst for zinc-air batteries driven overall water splitting," *Applied Catalysis B: Environmental*, vol. 297, article 120405, 2021.

[49] X. Zhong, W. Yi, Y. Qu et al., "Co single-atom anchored on Co_3O_4 and nitrogen-doped active carbon toward bifunctional catalyst for zinc-air batteries," *Applied Catalysis B: Environmental*, vol. 260, article 118188, 2020.

[50] D. Chen, X. Chen, Z. Cui et al., "Dual-active-site hierarchical architecture containing NiFe-LDH and ZIF-derived carbon-based framework composite as efficient bifunctional oxygen electrocatalysts for durable rechargeable Zn-air batteries," *Chemical Engineering Journal*, vol. 399, article 125718, 2020.

[51] C. Lafforgue, F. Maillard, V. Martin, L. Dubau, and M. Chatenet, "Degradation of carbon-supported platinum-

group-metal electrocatalysts in alkaline media studied by in situ Fourier transform infrared spectroscopy and identical-location transmission electron microscopy," *ACS Catalysis*, vol. 9, no. 6, pp. 5613–5622, 2019.

[52] Q. Wang, L. Shang, R. Shi et al., "NiFe layered double hydroxide nanoparticles on Co, N-codoped carbon nanoframes as efficient bifunctional catalysts for rechargeable zinc-air batteries," *Advanced Energy Materials*, vol. 7, no. 21, article 1700467, 2017.